Planetary and Space Science 235 (2023) 105738

Contents lists available at ScienceDirect

Planetary and Space Science

journal homepage: www.elsevier.com/locate/pss

Deep learning-based asteroid surface temperature evaluation from disk-resolved near-infrared spectra for thermal excess correction

Leevi Lind [a,*], Antti Penttilä [b], Kimmo A. Riihiaho [a], Eric MacLennan [b], Ilkka Pölönen [a]

[a] University of Jyväskylä, Faculty of Information Technology, Mattilanniemi 2, Jyväskylä, 40100, Finland
[b] University of Helsinki, Department of Physics, P.O. Box 64, Helsinki, 00014, Finland

ARTICLE INFO

Keywords:
Asteroid
Near-infrared
Disk-resolved
Reflectance spectroscopy
Thermal excess
Neural network

ABSTRACT

Near-Earth asteroids can become warm enough to emit radiation at near-infrared wavelengths, close to 2.5 μm. Thermal radiation can interfere with reflectance measurements in these wavelengths, and should be evaluated and corrected for. Current methods for correcting disk-resolved measurements either rely on previous Earth-based observations or perform heavy computations to find the thermally emitted spectral radiance. Using results based on disk-integrated observations may lead to errors for some cases where the target asteroid surface is not homogeneous. Computational efficiency is desirable for those future missions where data processing is to be performed on-board the spacecraft due to a limited downlink budget, such as missions employing small spacecraft. We propose to predict the temperature of an asteroid surface element from its observed spectral radiance using a convolutional neural network. The thermal spectral radiance emitted by the asteroid surface can be approximated using the temperature, and subsequently subtracted from the original spectral radiance. The model was tested using OSIRIS-REx measurements of asteroid (101955) Bennu with promising results. The performance of the model should be validated further in the future as asteroid missions produce suitable data. Both accuracy and speed of the method could likely be increased significantly with further development.

1. Introduction

One of the methods for characterizing asteroid surface composition is reflectance spectroscopy: measuring the amount of sunlight reflected from the asteroid's surface as a function of wavelength and looking for features characteristic to minerals and other materials, and surface properties (Gaffey, 1993; DeMeo et al., 2009; Binzel et al., 2019). Asteroids are, by definition, small compared to planetary bodies. Typically only disk-integrated observations are possible from Earth or its vicinity: the target is seen as an unresolved point of light. Disk-resolved measurements, which allow the detection of spatial variations, usually require close exploration by robotic spacecraft. Recent high-profile examples of such asteroid missions include the JAXA Hayabusa2 to asteroid (162173) Ryugu (Kitazato et al., 2019) and the NASA OSIRIS-REx to (101955) Bennu (Simon et al., 2020). While the main objective of both missions was returning a sample of asteroid regolith to Earth, they also mapped the reflectance properties of their targets to provide context for the retrieved sample.

The near-infrared (NIR) region of wavelengths (definitions vary, but in this study NIR refers to approximately 1–3 μm) covers spectral signatures important for mineralogical analysis of asteroids (DeMeo et al., 2009; Gaffey, 1993). For example, the reflectance of pyroxene has prominent absorption features at the wavelengths of 1 μm and 2 μm (Gaffey, 1993). Analyzing spectroscopic data from this wavelength range can be problematic due to an overlap in reflected sunlight and thermal emission from the asteroid's surface. As an asteroid absorbs sunlight its surface gets warmer. This moves the thermal emission toward shorter wavelengths, and for sufficiently warm asteroids a significant thermal contribution can be found in the NIR region. This thermal emission coincident with reflected light is known as thermal excess.

The overlap of reflected light and thermal emission in NIR observations of asteroids is a known and documented property. Rivkin et al. (2005) evaluated that in disk-integrated measurements thermal flux could contribute up to several tens of percent of the flux detected from a near-Earth object (NEO) at 2.5 μm wavelength. This thermal excess is larger for darker objects closer to the Sun. The overlap of reflected and thermally emitted light is both a problem and an opportunity. If the presence of thermal emission is not recognized and evaluated correctly, it

* Corresponding author.
E-mail addresses: leevi.j.j.lind@jyu.fi (L. Lind), antti.i.penttila@helsinki.fi (A. Penttilä), kimmo.a.riihiaho@jyu.fi (K.A. Riihiaho), eric.maclennan@helsinki.fi (E. MacLennan), ilkka.polonen@jyu.fi (I. Pölönen).

https://doi.org/10.1016/j.pss.2023.105738
Received 11 February 2023; Received in revised form 5 May 2023; Accepted 12 June 2023
Available online 5 July 2023

can cause large errors in reflectance spectra. On the other hand, if the thermal contribution is evaluated correctly, it can offer additional information about the asteroid. In disk-integrated spectral measurements the thermal excess can be used to constrain the albedo and diameter of an asteroid (Reddy et al., 2012).

The thermal excess or thermal tail can naturally also be present in disk-resolved NIR measurements of asteroids. Spectral measurements from both OSIRIS-REx and Hayabusa2 required correction for thermal emission to each observed spectrum in order to accurately evaluate the spectral reflectances of their targets. For Hayabusa2 NIRS3 instrument (Iwata et al., 2017) data the correction was made with two methods, yielding results that were in good agreement. Both approaches relied on global properties of the target asteroid Ryugu: the first method used an albedo derived from ground-based measurements, and the second a global reflectance trend established from NIRS3 measurements (Kitazato et al., 2019). For OSIRIS-REx's OVIRS instrument (Reuter et al., 2018) several correction schemes were tested with data measured using OVIRS, and the best-performing one was selected. This method involved fitting 325 thermal radiance spectra of different temperatures to each observed spectral radiance, and selecting one of them by minimizing a criterion for the best fit (Simon et al., 2020).

An overlap of reflected sunlight and thermal emission was also detected in measurements of (1) Ceres and (4) Vesta made with the VIR instrument (De Sanctis et al., 2011) of the NASA Dawn spacecraft. In Tosi et al. (2014), a Bayesian method for retrieving the surface temperature and emissivity was applied to VIR data from Vesta. For each analyzed spectrum, the authors constructed a synthetic spectral radiance in the wavelength range from 4.5 μm to 5.1 μm by summing modeled spectral radiances for thermal emission and reflected sunlight. They then fit this synthetic spectral radiance to the observed spectral radiance with a Bayesian optimization process, using the surface temperature and spectral emissivity as fitting parameters. After retrieving the temperature through this fit, the authors performed a second Bayesian fitting for shorter wavelengths by keeping the temperature fixed and using only the spectral emissivity as a free parameter. The Bayesian approach to retrieving thermal properties allowed the authors to include preliminary estimates of temperature and emissivity into the optimization process as starting guesses. The method presented in Tosi et al. (2014) was based on an earlier approach to the same problem. In Keihm et al. (2012) the authors used a similar method to analyze the thermal properties of (21) Lutetia, observed during a fly-by of the ESA Rosetta spacecraft.

In both Raponi et al. (2019b) and Raponi et al. (2019a), surface temperatures and emissivities of different areas of Ceres were found from VIR data through a fitting process. The authors modeled the sum of thermally emitted and reflected spectra, and fit the model to each observed spectrum using as free parameters not only the temperature and emissivity, but also several parameters related to the reflection properties and composition of the surface. The thermal properties and the reflection properties of the surface were retrieved simultaneously through one iterative fitting process.

Beyond the correction of reflectance spectra, maps of surface temperature and emissivity are useful for the thermal modeling of asteroids. A temperature map enables determining the thermal inertia of the surface material. This property, which describes a material's ability to resist temperature change, is closely connected to the physical properties of the surface material, for example the size of the regolith grains (Delbo et al., 2015). Temperature maps have been used to find thermal inertia values from Rosetta VIRTIS measurements of Lutetia (Coradini et al., 2011) and Steins (Leyrat et al., 2011), and from DAWN VIR measurements of Ceres (Rognini et al., 2020) and Vesta (Tosi et al., 2014).

One future mission where the overlap of thermal emission and reflected light may play a role is ESA Hera, the European component of the Asteroid Impact and Deflection Assessment (AIDA). The aim of AIDA is to test a deflection technique for potentially hazardous asteroids by driving a kinetic impactor to the moon of a binary asteroid and examining the change in its orbit. AIDA consists of two missions: the impactor, NASA Double Asteroid Redirection Test (DART) (Rivkin et al., 2021) which collided with its target in September 2022, and Hera (Michel et al., 2022), which will arrive in December 2026 to examine the aftermath of the collision. The target of AIDA is the binary asteroid (65803) Didymos, and DART collided with Dimorphos, the satellite of the primary body.

Hera, set to launch in 2024, is a mission for both science and technology demonstration. Hera will carry two CubeSats, Juventas (Goldberg et al., 2019) and Milani (Ferrari et al., 2021), which will be deployed in the vicinity of Didymos. The three spacecraft will set up a communication network between them and work in concert to examine their target asteroid. Milani's primary scientific payload is the ASPECT imaging module. ASPECT consists of four separate spectral instruments, each covering a different wavelength range with a spectral resolution of approximately 20 nm in the visual wavelengths, and approximately 40 nm in infrared. The different ranges have slight overlap, allowing construction of continuous spectra from 0.5 μm to 2.5 μm. ASPECT is tasked with mapping the reflectance properties of both Didymos and its satellite Dimorphos (Michel et al., 2022). According to thermophysical modeling of the Didymos system (Pelivan et al., 2017), an overlap of reflected sunlight and thermal emission may be present in the longer end of ASPECT's wavelength range. Producing reliable reflectance results with data from ASPECT requires assessing the thermal emission and removing it. In this work, we examine the challenge of correcting spectral radiances for thermal excess found in ASPECT's wavelength range. We also consider how data from possible future missions carrying similar instruments could be corrected for the same errors.

The correction methods used for NIRS3 data of Ryugu relied on global properties of the target. One of the methods made use of the albedo, and the other assumed the linearity of an area of the reflectance spectrum. In the Didymos system, the most interesting element will be the crater created by the DART collision. This is a relatively small area that could differ significantly from the rest of the surface of both Didymos and Dimorphos. The small crater area will be overshadowed by the bulk of the asteroid in disk-integrated observations, and thus relying on such measurements for corrections may lead to errors. Similarly, establishing a global reflectance trend, as was done with corrections of OVIRS data of Bennu, could invite errors when variation in the reflectance is expected.

The method used to analyze data from Ceres in Raponi et al. (2019b) and Raponi et al. (2019a) also relied on prior knowledge of the target. The approach requires a shape model of the asteroid and laboratory spectra of minerals that are expected to be present on the surface. The method described in Tosi et al. (2014) is also mentioned to make use of a shape model, but the authors note that omitting the photometric correction which utilized the shape model led to only small errors in temperature estimates. Neither of these methods treats the emissivity as constant, but instead they tie it to the spectral reflectance.

The method used for correcting OVIRS data in Simon et al. (2020) includes fitting 325 different functions to each observed spectrum and then selecting the best fit. The methods for analyzing data from Ceres in Raponi et al. (2019b) and Raponi et al. (2019a), from Vesta in Tosi et al. (2014), and from Ryugu in Kitazato et al. (2019) are also built on iterative fitting processes. The computational cost of fitting functions to thousands of measured spectra is not an issue when the data is streamed back to Earth where processing power is plentiful. However, missions employing small satellites such as CubeSats could benefit from processing the data from their instruments further on the spacecraft's on-board computer (OBC) Bruhn et al. (2020). The power of transmission equipment on such spacecraft is limited, also limiting the speed of downloading data back to Earth. More extensive processing on the OBC could reduce the volume of data needed to send back to Earth, as only ready data products can be downloaded instead of all raw data captured with instruments. The processing power available for a computer placed in a small spacecraft is limited, making computationally efficient methods desirable. Extensive on-board computations are not planned for Hera's Milani which can relay its data to Earth through the main Hera spacecraft. For missions where a CubeSat is to work alone, such as ESA's

planned M-ARGO mission (Walker et al., 2018; Topputo et al., 2021), these considerations could be more relevant.

Our proposed method of correcting disk-resolved radiance measurements for thermal emission relies on deep learning. Deep convolutional neural networks (CNN) have in recent years been used to predict many quantities from remotely sensed spectral data, for example the chlorophyll content of trees (Annala et al., 2020), water quality parameters (Hakala et al., 2020), and also mineral composition of asteroids (Korda et al., 2023). While neural networks are notorious for the amount of computational resources needed to train them, producing predictions with a trained neural network is not as demanding. We feed an observed spectral radiance, a sum of reflected and thermal components, to a deep learning model as input, and take the temperature of the observed surface element as an output. Together with an estimated emissivity, the temperature can be used with Planck's law to estimate the thermally emitted spectral radiance. This spectrum can then be subtracted from the original observed radiance to find the reflected spectral radiance. This study aims to answer the following questions:

1. Can a CNN be used to predict asteroid surface element temperature from disk-resolved spectral radiances with wavelength range of 0.5–2.5 μm?
2. Can such temperature predictions be reliably used to correct the spectral radiance observations for thermal excess?
3. How well would this temperature evaluation and correction method generalize for any asteroid mission employing a near-infrared spectral imager?

Implementing a neural network solution requires designing an architecture for the network, as well as preparing large amounts of data for the training phase. These are described in Sec. 3 together with our approach to testing the network. The results of these tests are presented in Sec. 4, and their implications are discussed in Sec. 5. Finally, conclusions are drawn in Sec. 6.

2. Materials and methods

Employing artificial neural networks and other machine learning methods in the analysis of astronomical data is not a new development. With its large data volumes, astronomy was one of the first fields to utilize these tools in automating data-analysis tasks in the 1980s (Ball and Brunner, 2010). Applying deep learning to asteroid spectra has likewise been done before this study, for example in Penttilä et al. (2021). We assume the reader is already familiar with the general principles of deep learning; for a more complete treatment of the subject, we refer the reader to Goodfellow et al. (2016).

Our problem can be described as that of regression: using a model to predict a continuous quantity from an input. The neural network used in this study belongs in the broad category of feedforward networks, where information flows only in one direction, from an input layer to an output layer through hidden layers in between. The hidden layers of the employed model consist of a block of 1D convolution layers followed by a block of fully connected (also called dense) layers. This further classifies our model as a convolutional neural network. The network was trained with a supervised learning scheme, where each output of the network was compared to a ground truth value using a loss function.

This section will describe the data used in training and testing of our deep learning model, the architecture of the model, and the implementation. The program code and weights for the trained neural network are available on GitHub at https://github.com/silmae/AsTherCorNN.

2.1. Data

Training an artificial neural network requires training data. This data should represent the real task the network is designed to solve as well as possible. Additionally, in our scheme of supervised learning, a ground truth corresponding to each training sample is required for evaluating the performance of the network during training and optimizing the weights of the network based on the evaluation.

We wish to infer asteroid surface element temperature from an observed spectral radiance. Thus, the training data should be observed spectral radiances, and the ground truth their associated temperatures. Ideally, the training data would consist of disk-resolved spectral radiance measurements of a wide variety of asteroids with different spectral properties and orbits, measured with several phase angles. The measured asteroids should also be warm enough to have noticeable thermal emission at NIR wavelengths shortward of 2.5 μm.

Unfortunately, a dataset corresponding to these specifications does not currently exist. Spacecraft missions to asteroids have been relatively few, and even fewer are those that produced both surface temperatures and approximately continuous spectral radiances in our wavelength region of interest, 0.5 μm–2.5 μm.

While individual datapoints from suitable missions are plentiful, using data from only a few asteroids to train our network would not make for a well-generalizable model. During training the model would learn to predict for reflectance profiles present in the training data, and would most likely give erroneous predictions when applied to asteroids outside of the training population. Instead of training with observed spectra, we opt to generate the training data through simulation and use measured data only for testing the trained network.

Specifications for data suitable for testing our method are largely the same as those for training data. The JAXA Hayabusa NIRS instrument did not reach far enough into infrared with its wavelength range extending from 0.76 to 2.25 μm (Kitazato et al., 2008), while the Hayabusa2 NIRS3 instrument ranging from 1.8 to 3.2 μm lacked shorter wavelengths (Iwata et al., 2017). The NASA NEAR-Shoemaker NIS instrument data from Eros is closer with wavelengths from 0.8 to 2.5 μm, but the spacecraft did not have a thermal instrument to provide ground truth temperatures corresponding to the spectra (Prockter et al., 2002). Data from Dawn's VIR would have a suitable wavelength range and temperatures derived from the same data, but the target asteroids of the mission were not warm enough to manifest significant thermal emission in the wavelength range we are interested in. Spectra from Ceres are reported to have thermal emission starting at 3.2 μm (Raponi et al., 2019a, 2019b), and those from Vesta starting at 3.5 μm (Tosi et al., 2014). Observations of Lutetia and (2867) Steins made by the Rosetta VIRTIS instrument during flybys have the same problem. Thermal emission from Steins starts to become prominent longward of 4 μm (Leyrat et al., 2011), and from Lutetia longward of 3.5 μm (Keihm et al., 2012).

Finally, observations of Bennu made with the OSIRIS-REx OVIRS instrument match all our criteria. The wavelength range extends from 0.4 to 4.3 μm, each spectrum is accompanied by estimated values for temperature and emissivity, and a noticeable thermal contribution is present under the wavelength of 2.5 μm (Simon et al., 2020). We will use data from these observations for testing our method.

In the following treatment where we describe the simulator used for generating training samples, we denote the wavelength of electromagnetic radiation with λ, and mark all spectral quantities with the subscript λ. We can describe the observed spectral radiance L_λ as a sum of reflected sunlight and thermal emission:

$$L_\lambda = L_{R,\lambda}(I_{\odot,\lambda}(d_\odot), R_\lambda, p, \theta_i, \theta_e) + L_{T,\lambda}(T, \epsilon), \tag{1}$$

where $L_{R,\lambda}$ denotes reflected spectral radiance, and $L_{T,\lambda}$ denotes thermally emitted spectral radiance (Hapke, 2012). In our model the reflected radiance depends on five parameters: incident collimated spectral irradiance from the Sun $I_{\odot,\lambda}(d_\odot)$, spectral reflectance R_λ and visual geometric albedo p of the body, the incidence angle of sunlight θ_i, and the emission angle of reflected light θ_e. The incidence and emission angles are measured from the local surface normal. An azimuth angle between the directions of incident and reflected light is not required, as our simple model does not account for azimuthal effects.

Radiance reflected towards an observer from a surface element is given by multiplying the incident collimated spectral irradiance $I_{\odot,\lambda}(d_\odot)$ with the bidirectional reflectance r_λ of the surface:

$$L_{R,\lambda} = I_{\odot,\lambda}(d_\odot) r_\lambda. \tag{2}$$

The incident spectral irradiance at any heliocentric distance $d_\odot$ can be calculated by taking the solar spectral irradiance outside Earth's atmosphere at an approximate heliocentric distance of 1 au, and scaling it with the square of the heliocentric distance in astronomical units:

$$I_{\odot,\lambda}(d_\odot) = I_{\odot,\lambda}(1\ \text{au})/d_\odot^2. \tag{3}$$

The bidirectional reflectance r_λ was calculated using the Lommel-Seeliger model of reflection (Shepard, 2017),

$$r_\lambda = \frac{w_\lambda}{4\pi} \frac{\cos\theta_i}{\cos\theta_i + \cos\theta_e}, \tag{4}$$

where w_λ denotes the spectral single-scattering albedo, and θ_i and θ_e are the incidence and emission angles, respectively. The Lommel-Seeliger model allows for each photon only one interaction with the surface medium: either scattering or absorption. The single-scattering albedo describes the probability of a scattering event occurring in this single interaction. The Lommel-Seeliger model also gives a relationship between the single-scattering albedo and geometric albedo of a perfectly spherical body:

$$w = 8p. \tag{5}$$

In our model, this law is used for spectral quantities as $w_\lambda = 8p_\lambda$. The spectral geometric albedo p_λ was calculated by multiplying the visual geometric albedo by the normalized reflectance spectrum, as $p_\lambda = pR_\lambda$. The visual geometric albedo is measured at approximately 0.55 μm wavelength, and in the normalization of asteroid reflectance spectra this wavelength is set to unity: multiplying the two yields an "un-normalized" reflectance spectrum, or spectral geometric albedo.

For simulating thermally emitted spectral radiance $L_{T,\lambda}$ our model employs Planck's law weighed with an emissivity ϵ:

$$L_{T,\lambda} = \frac{2hc^2}{\lambda^5} \frac{1}{\exp\left(\frac{hc}{\lambda k_B T}\right) - 1} \epsilon. \tag{6}$$

Here h is the Planck constant, c is the speed of light in vacuum, λ is the wavelength, k_B is the Boltzmann constant, and T is the temperature. Planck's law describes the thermally emitted spectral radiance from an ideal blackbody. To make this spectrum more representative of a non-ideally emitting asteroid, each produced spectrum was multiplied by an emissivity, a constant value between 0 and 1.

The reason for using an emissivity that is constant with respect to wavelength is to mimic our test data consisting of OVIRS measurements of Bennu, which were corrected for thermal emission with a constant emissivity. The approximated emissivities used for correcting OVIRS data are not true emissivities, as they also include effects caused by surface geometry (Simon et al., 2020). In this too, our data generation follows the same approach. Treating emissivity as a constant rather than a spectrum at near-infrared wavelengths has met with some criticism (Myhrvold, 2018), but we feel it is justified in this case. Training the neural network with data created using spectral emissivities would make the network perform worse with the test data.

Our model requires eight parameters to simulate one datapoint: temperature T, emissivity ϵ, heliocentric distance $d_\odot$, solar spectral irradiance at 1 au $I_{\odot,\lambda}(1\ \text{au})$, geometric albedo p, normalized reflectance spectrum R_λ, and incidence angle θ_i and emission angle θ_e measured from the local surface normal. Out of these only the solar irradiance and the reflectance spectrum are based on measurements. The spectral irradiance outside Earth's atmosphere at approximately 1 au heliocentric distance was retrieved from the website of the National Renewable Energy Laboratory of the United States as the ASTM Standard Extraterrestrial Spectrum Reference E−490-00 (Spectrum Reference e-490-00).

The used asteroid reflectance spectra come from a dataset described in Penttilä et al. (2021), specifically designed for machine learning purposes. The data originate from two previous asteroid reflectance datasets, the Bus-DeMeo dataset (DeMeo et al., 2009) and the MITHNEOS dataset (Binzel et al., 2019). To balance the number of samples in different classes and create more data, the authors of Penttilä et al. (2021) synthesized more spectra using an approach based on principal component analysis. Artificially generating more data from existing samples is a common approach to improving the performance of a machine learning model; this procedure is known as dataset augmentation (Goodfellow et al., 2016). Spectra in the reflectance dataset had a wavelength range of 0.45–2.45 μm, with 200 spectral channels at equal intervals. This same wavelength vector was used in all our computations, interpolating other spectral data to match it. We considered this range to be sufficiently close to the wavelength range of the ASPECT imaging module, which operates between 0.5 μm and 2.5 μm.

The reflectance dataset consisted of normalized asteroid spectra, with the wavelength channel at 0.55 μm set to unity. The data also included the spectral class of each sample. Our model for simulating reflected radiance requires geometric albedos to convert the normalized spectral reflectances into spectral geometric albedos. Mean albedos of the spectral classes present in the data were retrieved from DeMeo and Carry (2013) for classes A, B, C, D, K, L, Q, S, and V, and from Ryan and Woodward (2010) for classes T and X. However, these did not appear representative of all asteroids: the albedo of Bennu, classified as a B-type asteroid (Bennu on Small-Body Database), differed significantly from the mean albedo of its spectral class. Bennu's geometric albedo is listed in the Small-Body Database as 0.044, while DeMeo and Carry (2013) gives the mean albedo of the B-class as 0.14 ± 0.04. Instead of using the mean albedo of each spectral class for the samples belonging to it, the geometric albedos were pulled randomly from a uniform distribution. The minimum and maximum limits for the random albedos broadly followed the minimum and maximum of the mean albedos retrieved from DeMeo and Carry (2013) and Ryan and Woodward (2010), with minimum albedo being 0.01, and maximum 0.40. These are listed along with other minimum and maximum parameter values of data generation in Table 1.

The single-scattering approximation central to the Lommel-Seeliger model of reflection is not well suited for brighter surfaces (Shepard, 2017). In fact, the single-scattering albedos in our model often significantly exceed the physical limit of 1, resulting in surface elements that reflect more light than is incident on them. While this would seem alarming, it is roughly equivalent to having a surface with an albedo of 1 closer to the Sun where there is more incident light to reflect. The form of Lommel-Seeliger model is also only applicable to flat surfaces, which asteroid surface regolith is not, and it does not take into account the opposition surge or other effects related to the phase angle of the observation.

While the data generation model makes many simplifications, it appears to describe the problem of overlapping reflection and thermal emission accurately enough: when a neural network is trained using generated data, the network can produce useful predictions from real, measured data. The data generation model also has merit in easy implementation and low computational cost. The simplicity of the model allows the data to be generated in a reasonable time on a comparatively low-end computer. Generating the dataset utilized in this study took

Table 1
Minimum and maximum parameter values used in generating the training and validation data.

Parameter	T [K]	ϵ	$d_\odot$ [au]	p	θ_i[°]	θ_e[°]
Min.	300	0.20	0.797	0.01	0	0
Max.	441	0.99	1.456	0.40	89	89

approximately half an hour using a consumer-grade laptop.

As data from Bennu was selected for testing the model, cases present in the training data were constrained to fit the conditions on Bennu. Though Bennu is a well characterized body, we used only its orbital characteristics for limiting the data generation parameters. Bennu's perihelion and aphelion (approx. 0.897 and 1.356 au, respectively, retrieved from the Small-Body Database (Bennu on Small-Body Database)) were used for the minimum and maximum heliocentric distances when generating reflected radiances. To account for approximation errors in our models, a margin was added to the range of distances by subtracting 0.1 au from the perihelion and adding 0.1 au to the aphelion. A maximum value for temperature was calculated from the minimum heliocentric distance by finding the maximum temperature of an object placed at that distance from the Sun, when the object is in equilibrium with sunlight. The temperature of such an object can be calculated using the following equation (Hapke, 2012):

$$T = [(1 - A)I_{\odot}(d_{\odot})\cos\theta_i/\epsilon\sigma]^{1/4}. \tag{7}$$

Here A is the Bond albedo of the object: the fraction of incident electromagnetic radiation that is scattered into space upon interaction with the body, integrated over all wavelengths and directions. $I_{\odot}(d_{\odot})$ is the incident solar irradiance from all wavelengths at the heliocentric distance of $d_{\odot}$, θ_i is the incidence angle of sunlight, ϵ is the emissivity of the object, and σ is the Stefan-Boltzmann constant. To find the maximum temperature, we consider the subsolar temperature T_{ss} where $\theta_i = 0$, and treat the object as a perfect blackbody with $A = 0$ and $\epsilon = 1$. This simplifies the expression for the temperature to

$$T_{ss} = [I_{\odot}(d_{\odot})/\sigma]^{1/4}. \tag{8}$$

The incident irradiance was found by taking its value near Earth at 1 au (1361 W/m^2 (Kopp and Lean, 2011)) and scaling it with the inverse square law similar to Eq. (3) used for spectral irradiances. For Bennu's perihelion with the subtracted margin of 0.1 au, calculation using Eq. (8) yielded a maximum temperature of 441 K.

To find a suitable value for the minimum temperature, the data generation model was used to evaluate how surface temperature affects the radiance caused by thermal emission in an example case. The percentage of thermally emitted radiance out of total detected radiance at the wavelength channel closest to 2.45 μm was modeled at 1 au heliocentric distance with temperatures running from 250 K to 350 K. The radiances were modeled with a standard viewing geometry of 30° incidence angle and 0° emission angle, and three values of geometric albedo, 0.02, 0.05, and 0.08. Emissivities of the three modeled surface materials were calculated from the albedo values through Kirchhoff's law (Modest, 2013):

$$\varepsilon'(\theta) = 1 - r'^{\supset}(\theta), \tag{9}$$

where $\epsilon'(\theta)$ denotes directional emissivity with emission angle of θ, and $r'^{\supset}(\theta)$ denotes directional-hemispherical reflectance with incidence angle of θ. The directional-hemispherical reflectance of a Lommel-Seeliger surface can be found from the single-scattering albedo w as (Shepard, 2017):

$$r'^{\supset}(\theta) = \frac{w}{2}\left[1 - \cos\theta \ln\left(1 + \frac{1}{\cos\theta}\right)\right]. \tag{10}$$

The single-scattering albedo can be calculated from the geometric albedo using Eq. (5).

A plot of the results for the example case can be seen in Fig. 1, showing the percentage of thermal emission as a function of temperature. Based on the figure, the temperature of 300 K was set as the minimum for the training data. At this temperature the thermal contribution was approximately one percent in the most extreme case of 0.02 albedo.

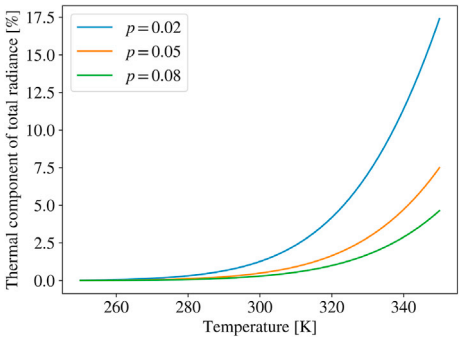

Fig. 1. Percentage of thermal emission out of total detected radiance at 2.45 μm wavelength, presented as a function of surface temperature. Three example cases with different geometric albedos p were modeled at 1 au heliocentric distance, with 30° incidence angle and 0° emission angle.

The workflow for creating the radiance datasets for training and validation is illustrated in the diagram of Fig. 2. Creation of the dataset began with shuffling the reflectance dataset and splitting it into training and validation sets, with 90% of the available 2200 spectra used for training, and 10% for validation. Next, each of the normalized spectra was "un-normalized" with five different random values of geometric albedo pulled from a uniform distribution, giving five spectral geometric albedos from each normalized reflectance. In total this yielded 9900 spectra used for creating training data and 1100 spectra for test data. A vector of temperatures was then created, running from the minimum of 300 K to the maximum of 441 K, with a step of 1 K. For each temperature, 3960 training radiances and 440 validation radiances were created according to Eq. (1), simulating the reflected and thermally emitted radiances separately and summing them. The procedure of creating training samples and validation samples differed only in the number of samples per temperature value, and in the used pool of spectral geometric albedos. Gaussian noise with a mean value of 0 and standard deviation of 0.0001 was generated and added to each sum radiance spectrum; this was done to make sure there were no identical samples in either dataset, and to make the neural network robust against small amounts of noise in the input spectra. In total the generated data amounted to 558 360 radiances for training and 62 040 radiances for validation, and their corresponding ground truth temperatures.

Data used in testing the model consisted of measurements of the asteroid Bennu, recorded with the OVIRS instrument (Reuter et al., 2018) of the OSIRIS-REx mission. OVIRS is a point spectrometer with a wavelength range of 0.4 μm–4.3 μm, calibrated to record spectral radiances. During the mission, this instrument was used in a whiskbroom configuration, sweeping the field of view over the asteroid to map its surface properties. In the paper that introduced OVIRS, Reuter et al. (2018), the correction for thermal emission was mentioned to rely on temperature evaluations produced with a longer wavelength instrument, OTES (Christensen et al., 2018). The data we used for this study is described in detail in Simon et al. (2020), where the depiction of the thermal correction is different from the earlier publication. The correction began with trial runs for five competing methods, conducted using multiple large datasets from OVIRS. The best-performing method modeled the reflected spectral radiance by approximating the reflectance of Bennu as a linear continuum with a slope defined by fits to data from Bennu. The reflected radiance produced using this approximation and scaled to match the observed spectral radiance was then subtracted from the observed spectrum, leaving an approximation for the thermally emitted radiance. Next, 325 thermal spectral radiances were generated using Planck's law with temperatures ranging from 150 K to 475 K, with a step of 1 K. Each of these was fitted to the approximated thermal radiance spectrum using a scaling factor as a fitting parameter. The final thermal radiance spectrum was selected among the 325 spectra by minimizing a criterion for the goodness of fit. Besides the thermally emitted spectral

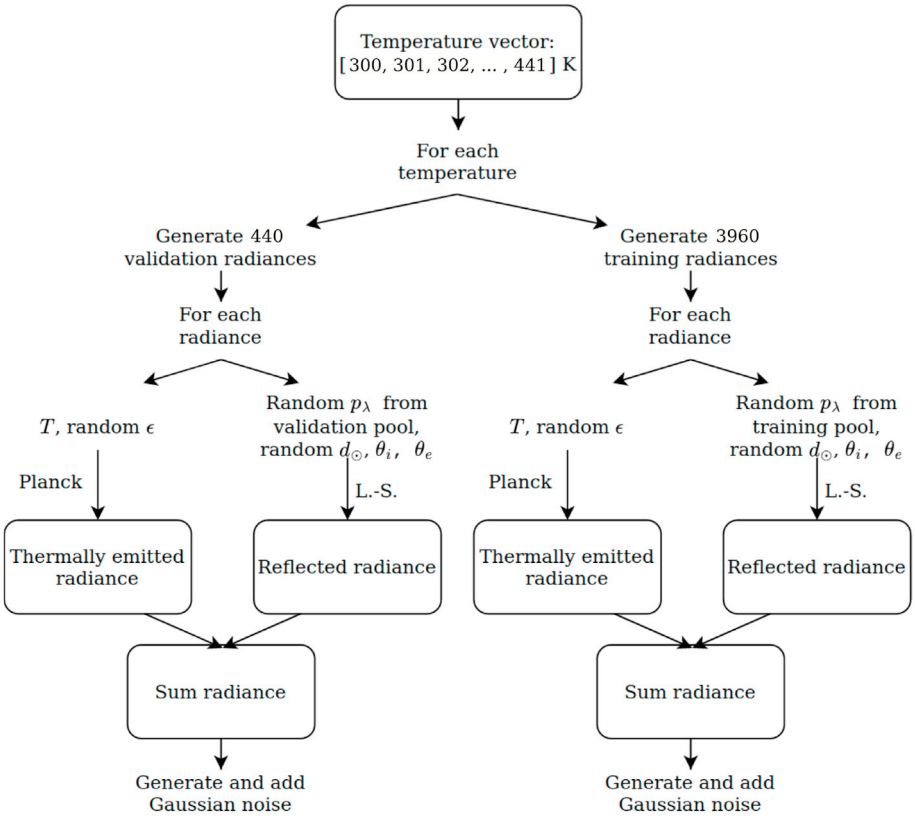

Fig. 2. Workflow for creating the training and validation datasets.

radiance, the method yielded an estimation for the surface temperature, and an emissivity-like parameter with directional effects of the emitted radiance built into it. A more thorough description of the correction can be found in the supplementary materials of Simon et al. (2020).

The data for each observation comprised uncorrected spectral radiance, thermal tail spectral radiance, corrected spectral radiance (with the thermal tail subtracted), surface temperature, and emissivity. The data originated from three local times on Bennu, namely 10:00, 12:30, and 15:00, and were grouped by the time of observation. In some of the measurements, the sensor's field of view was not pointing toward Bennu. These measurements were identified and discarded by setting a threshold value for spectral radiance integrated over the wavelengths, calculating the integrated radiance for all uncorrected radiances, and discarding any measurement that fell below the threshold. The spectral radiances of the surviving measurements were plotted and manually examined for bad fits. In some samples, something appeared to have gone wrong when a continuous spectrum was created by stitching together spectra from sensors with different wavelength ranges. This manifested as a region of higher radiance between approximately 0.7 μm and 1.1 μm, with an extremely sharp rise and drop at the ends of this range. Measurements where this behavior was detected were also discarded, leaving in total 1219 data points for testing. These were made compatible with the correction method by converting the spectral radiances to the unit W/(m^2 sr μm) and interpolating them to match the wavelength vector of the training data.

If our correction method were to be used for real data, it could encounter temperatures lower than the minimum present in the training data. To test how the neural network behaves with such samples, another synthetic test dataset was created. As in previous data generation, the modeled temperature values were created as a vector running from a minimum value to a maximum with a step of 1 K: only the minimum value was changed from the previous 300 K–150 K. The number of generated samples per temperature value was adjusted from 440 to 220 to keep the total number of created samples roughly the same. In total, this data comprised 64 020 samples.

2.2. Network architecture and implementation

Generating the data, implementing, training, and testing the deep learning model, and all other calculations were performed using Python 3.9.7 (Python 3.9.7 documentation). The model was built using TensorFlow (Abadi et al., 2015) with its Keras framework (Chollet et al., 2015). The optimal architecture for the model was determined with the Bayesian optimizer of KerasTuner (O'Malley et al., 2019), a hyperparameter optimization tool built for Keras.

The input data comprised spectral radiances with 200 wavelength channels, setting the input layer to be 200 nodes. The output was likewise determined by the context to be one node, for the predicted temperature value. Hidden layers of the network consisted of a block of 1D convolutional layers followed by a block of fully connected layers. A flatten layer was placed between the two blocks to render the output of the convolution compatible as an input to the following fully connected layer. The convolution block was set to consist of four layers in total, with filter counts of 128, 64, 32, and 16. Kernel width for the convolution operations was four, and padding was used to keep the output of each convolution the same size as the input. For the fully connected block, the optimization yielded a structure of nine layers with descending node counts from 1024 to 4, each layer halving the number of nodes of its predecessor. The activation function for all layers, excepting the output layer, was the rectified linear unit (ReLU) (Nair and Hinton, 2010). An illustration of the network architecture can be seen in Fig. 3.

The network was trained with a minibatch size of 32. The used optimizer was Keras's implementation of Adam (Kingma and Ba, 2017) with a learning rate of 5×10^{-5}, keeping other parameters of the optimizer at their preset values. The loss for each training output was calculated with Keras's native mean absolute percentage error (MAPE)

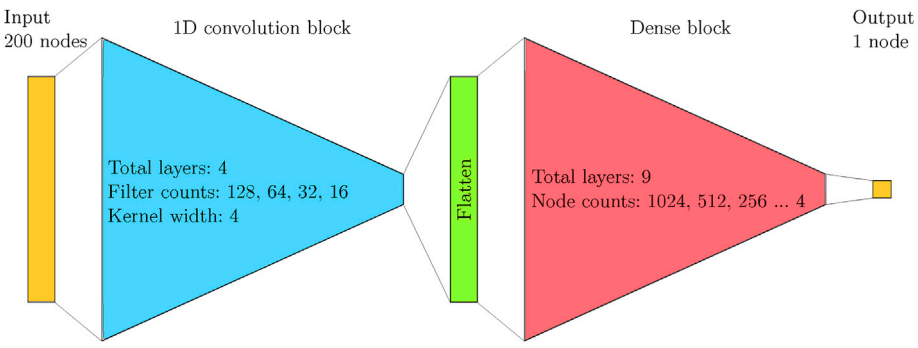

Fig. 3. Architecture of the used neural network.

loss function. The network was initially set to train for 1000 epochs in total, but a plot of training and validation loss history revealed overfitting after epoch 29: thus, the weights from this epoch were selected as the final weights of the network. The training was conducted using a single NVIDIA Tesla P100 graphics processing unit (GPU), and the 29th epoch was completed after 35 min of training.

2.3. Testing

The trained neural network was tested with three datasets: the synthetic validation data used during training to monitor network performance and generalizability, real OVIRS data from Bennu, and another synthetic dataset with a broader temperature range.

The testing procedure was identical for all three datasets. First, the whole dataset was fed to the network using Keras's evaluate method, and the loss and total prediction time for the dataset were recorded. Next, the network was used to predict a temperature for each radiance spectrum of the dataset. The temperature was used to produce a prediction for thermally emitted spectral radiance according to Eq. (6). The emissivity value used in the calculation was the mean emissivity of the produced synthetic data, 0.595. Subtracting the predicted thermal radiance spectrum from the input spectrum yielded a prediction for reflected radiance: a spectral radiance corrected for thermal tail using the network's temperature prediction. Both ground truth and predicted reflected radiances were turned into normalized reflectance spectra by dividing them by the solar spectral irradiance, and then normalizing both so, that the reflectance at 0.55 μm wavelength was 1.

To determine how successful a correction was, the corrected spectra were compared with ground truth. Comparisons were also made for the uncorrected spectra, to give context to the readings calculated for corrected points. The similarity of spectra was quantified with the metric of spectral angle, defined for two vectors x and y as (Kruse et al., 1993)

$$\cos^{-1}\left(\frac{x \cdot y}{\|x\| \cdot \|y\|}\right). \tag{11}$$

The spectra are treated as vectors in N-dimensional space, where N is the number of spectral channels. The spectral angle calculates the angle between the two vectors, ignoring possible differences in their magnitudes. In the case of spectra, this means that only relative differences of channels, i.e. the spectral shapes, are compared.

All test calculations, including using the neural network to make predictions, were carried out on a Dell Latitude 5420 laptop equipped with an Intel Core i7-1165G7 8-core central processing unit running at 2.80 GHz clock speed.

3. Results

Producing temperature predictions with the trained neural network was quite fast. For the synthetic validation data comprising 62 040 samples, the total elapsed prediction time was 34.1 s, making the prediction time per sample approximately 0.5 ms. Temperature predictions for the Bennu data were made in three batches, each corresponding to a local time when the measurements were made. Computation times for these predictions were slightly shorter, with a mean time per sample of approximately 0.4 ms.

Fig. 4 shows plots of temperature predicted by the neural network as a function of ground truth temperature for both synthetic validation data and test data from Bennu. The synthetic data is limited to the range of ground truth temperatures on Bennu. Predictions made from synthetic data are worse for samples of lower temperature. When the temperature is lower, there is less thermal radiance in the NIR wavelengths. The lower thermal contribution is more readily "drowned out" by reflected radiation, and the network can not properly quantify it in most of the synthetic samples. As a result, the network predicts for the ambiguous cases temperatures leaning toward the mean temperature of the training data, resulting in values higher than ground truth values. The same issue is not

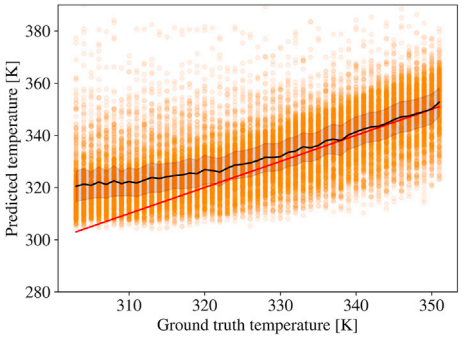

(a) Synthetic data

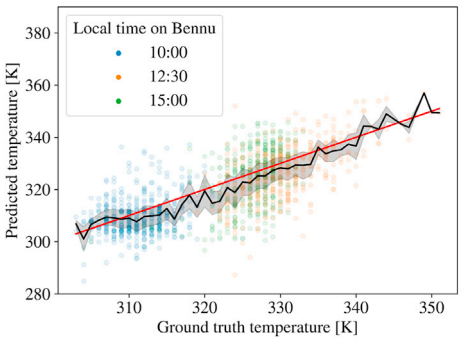

(b) Bennu data

Fig. 4. Predicted temperatures as function of ground truth temperatures, for both synthetic validation data and test data from Bennu. The red lines correspond to an ideal result. The black lines show the mean predicted temperature for each ground truth temperature, and the shadows around them show the standard deviations of the predictions.

present in the Bennu results, where the predictions for lower ground truth temperatures are not markedly worse than for higher temperatures. Compared to many of the training samples, data from Bennu are not as much affected by reflected radiation hiding the thermal component. Some temperatures predicted from Bennu data are lower than 300 K, the lower limit temperatures present in the training data. This points to differences between the training data and the test data from Bennu, which is to be expected. The rudimentary simulator used for creating the training samples can not accurately reproduce the complex real-world phenomena of reflection and emission from the surface of an asteroid.

Normalized reflectance spectra were calculated from both uncorrected and predicted reflected radiances, dividing them by the solar spectral irradiance and normalizing the result so that the reflectance at 0.55 μm equaled unity. Fig. 5 shows four results of spectral reflectance, two from synthetic data and two from Bennu data. In Fig. 5(a) the result is a successful correction from synthetic data: the predicted temperature differs from ground truth by 9.4 K, and the emissivity by 0.30. Still, the predicted reflectance conforms closely to the ground truth spectrum, with a spectral angle of 0.0003. In Fig. 5(b) we see the result of a less successful correction, where the temperature was predicted 16.3 K too high, and the emissivity missed its ground truth value by 0.31, resulting in a spectral angle error of 0.0149. The applied correction lowered the reflectance values in the NIR wavelengths too much, and the reflectance values for those wavelengths fell below the ground truth.

Fig. 5(c) shows a successfully corrected reflectance from Bennu data. The temperature prediction differed from the ground truth by only 1.8 K, and the emissivity by 0.09, giving a spectral angle error of 0.0010. A result from an unsuccessful correction is seen in Fig. 5(d), where the corrected spectrum is close to the uncorrected one. In this case the predicted temperature was 22.1 K too low, resulting in a too small thermal radiance. While the emissivity was correct, the temperature error caused a spectral angle error of 0.0100.

In some cases, the errors in temperature and emissivity predictions may also compensate for each other. If the temperature prediction is lower than the ground truth value, but the emissivity is higher than it should be, the predicted thermal radiance can come close to the ground truth spectrum. The same applies to cases where the temperature is predicted too high and the emissivity too low. On the other hand, the error in predicted radiance can be amplified if predictions of temperature and emissivity err in the same direction, i.e., both temperature and emissivity are either too high or too low.

Spectral angle errors of all reflectance predictions from the synthetic validation data and Bennu data are presented in Fig. 6. To improve the readability of the figures, some points of the synthetic data with larger errors in Fig. 6(a) were cropped out of the view. In both figures, the errors of most corrected points are smaller than those of uncorrected points. While the temperature predictions of synthetic samples with temperatures lower than 320 K were systematically too high, the error does not appear to propagate to reflectance predictions: most points are close to the ideal results of 0, with some outliers throughout the temperature range. The results from Bennu data show mostly similar behavior, with a majority of the corrected points close to 0. Near the temperature of 330 K some of the points show larger errors, and above 330 K the errors in general seem to increase. In general, the results for Bennu data are worse than for synthetic data.

Fig. 7 shows the predicted temperatures, an example reflectance correction result, mean spectral reflectances, and spectral angle errors of all reflectances for the broader temperature range of synthetic data, from 150 K to 441 K. As seen in the Bennu temperature range predictions of Fig. 4, the neural network is not capable of accurately predicting temperatures lower than approximately 320 K. Under 300 K the network appears to correctly recognize that the temperature is too low to produce significant amounts of thermal radiation. However, for most of the points the predicted temperature is not the lowest the network has encountered during training, 300 K. Rather, the predictions are centered around approximately 320 K. Interestingly, none of the predictions go below 300 K, unlike with some points of the Bennu data, seen in Fig. 4(b). Temperature predictions also seem to increase in error at the highest tested temperatures, showing lower values than ground truth. This could be caused simply by difficulty in predicting for the edges of the training data, suggesting that the maximum temperature of the training data should be higher than is likely to be encountered in real asteroid measurements.

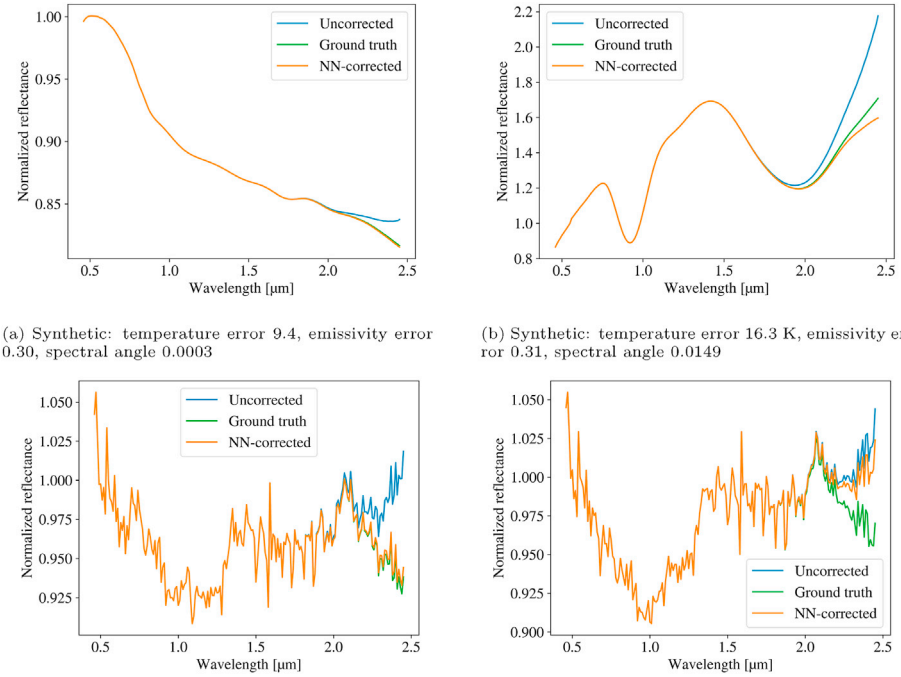

(a) Synthetic: temperature error 9.4, emissivity error 0.30, spectral angle 0.0003

(b) Synthetic: temperature error 16.3 K, emissivity error 0.31, spectral angle 0.0149

(c) Bennu: temperature error 1.8 K, emissivity error 0.09, spectral angle 0.0010

(d) Bennu: temperature error 22.1 K, emissivity error 0.00, spectral angle 0.0100

Fig. 5. Four different normalized reflectance predictions from synthetic and Bennu data, with uncorrected and ground truth spectra for comparison.

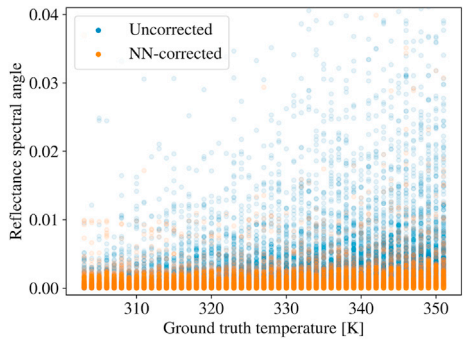

(a) Synthetic data

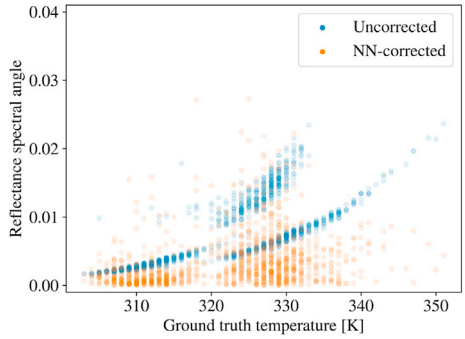

(b) Bennu data

Fig. 6. Spectral angles between corrected reflectance spectra and ground truth, and the same from uncorrected data for comparison.

Fig. 7(b) shows an example reflectance from a low temperature: the predicted temperature missed the ground truth by 93 K, and the emissivity by 0.29. However, the original thermal radiation was virtually nonexistent at NIR wavelengths, and the uncorrected and ground truth spectra overlap almost completely. The corrected spectrum is likewise in agreement with the ground truth, indicating that the subtracted thermal radiance was also very small.

While the network's temperature predictions for over half of the validation samples were far from the ground truth values, this did not affect the predictions of normalized reflectance very much, as seen in Fig. 7(c). The mean spectrum for corrected data follows the ground truth accurately, whereas uncorrected reflectance deviates strongly from it. For the purpose of correcting spectra for thermal emission, accurate predictions for the lower temperatures may not be needed: the emission to correct for is not obtrusive if the temperature is low. However, if the predicted temperature is much higher than the ground truth, applying the correction will result in an erroneous reflectance. The corrected mean reflectance spectrum following the ground truth quite accurately could also indicate that averaging the predictions of some samples could improve the results of corrections. As Fig. 7(a) shows, the predictions for each ground truth temperature are found both above and below the ideal result, yet the average prediction for higher temperatures is close to the ground truth.

Fig. 7(d) shows the spectral angle errors for all corrected and uncorrected points of the broader temperature range synthetic dataset. Apart from some noise, which is to be expected with a neural network, the corrected points below 300 K have mostly low errors. In very high temperatures over 400 K, the errors of corrected points rise significantly. This is caused by the erroneous temperature predictions in the same range, visible in Fig. 7(a). In high temperatures, a small error in a temperature prediction will sway the corrected spectrum more significantly.

4. Discussion

Results produced by the neural network were overall promising. For temperature predictions most of the errors occurred with lower temperatures, where the thermal emission is not as high at NIR wavelengths, and thus more difficult to characterize. For higher temperatures, the mean of predictions for each temperature matched the ground truth well, but deviation of the predictions from the mean was quite large throughout the temperature range.

While many of the temperature predictions were not ideal, using the

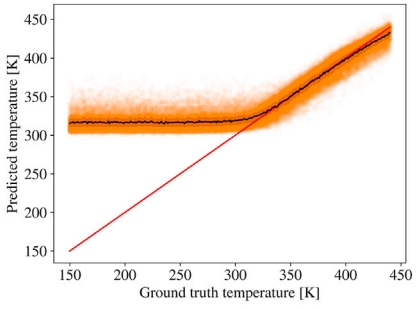

(a) Predicted temperatures

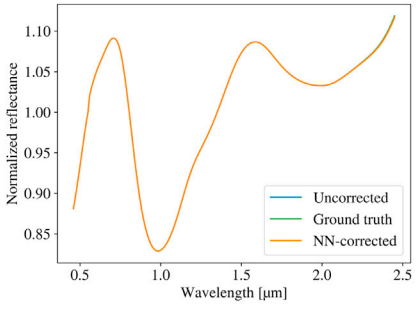

(b) Example reflectance: temperature error 93.0 K, emissivity error 0.29, spectral angle 0.0003

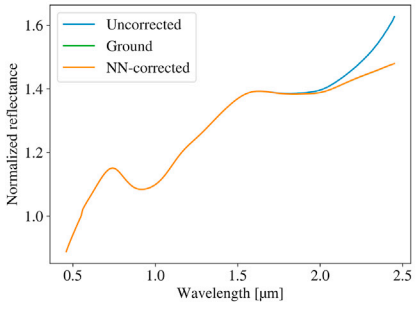

(c) Mean reflectances

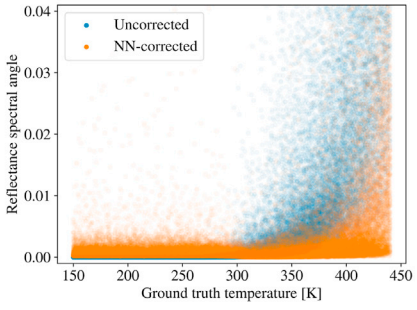

(d) Spectral angle of reflectance

Fig. 7. Predicted temperature as function of ground truth temperature (a), example reflectance (b), mean normalized spectral reflectance (c), and cosine distance errors (d) for the broader temperature range of synthetic validation samples. On the plot of temperature predictions the red line corresponds to an ideal result, while the black line shows the mean predicted temperature for each ground truth temperature, and the shadow around it shows the standard deviations of the predictions. On the example reflectance spectrum, the uncorrected, corrected, and ground truth spectra overlap, showing only the topmost corrected spectrum. The same is true for the mean reflectance spectra, where the ground truth is hidden by the corrected spectrum.

temperatures to correct spectral reflectances yielded encouraging results. The systematic errors seen in temperature predictions of synthetic low-temperature samples were not visible in reflectance corrections made with the same temperature predictions. It appears that even somewhat inaccurate temperature predictions can be used to correct NIR observations for thermal emission. Results from Bennu data were not as good as from synthetic data, pointing to differences between the two datasets.

Some outliers with large errors are present in predictions of both temperature and reflectance. This is likely to happen with a method based on a neural network. One way to detect these outliers could be to compare each temperature prediction to the mean of the predictions of neighboring pixels. Averaging the predictions of neighboring pixels could also be used to improve the deviation of the results, albeit at the cost of spatial resolution.

One large source of errors for reflectance predictions is the need for an emissivity value in addition to the temperature. Even with a temperature prediction close to the ground truth value, an error in emissivity can compromise the radiance prediction. Our neural network can not currently produce emissivity estimates, unlike the other methods for retrieving thermal properties we discussed in the introduction of this work. For the emissivity of all radiance predictions, we used simply the value halfway between the minimum and maximum emissivities of the training data. During the development of the neural network several architectures that would also predict the emissivity from the input radiance were tried, but with no results to speak of. Each network ended up to the same solution we later used, converging to predict the same emissivity for all inputs. Correct emissivity predictions could significantly improve the results of both radiance and reflectance predictions. Another likewise failed attempt to predict both temperature and emissivity was setting the output of a network to be the thermally emitted spectral radiance. The temperature and emissivity could then be evaluated by fitting the output to Planck's law. However, the output spectra of such networks were both erroneous and noisy.

The relatively good performance of the neural network with Bennu data can be partly attributed to Bennu being included in the original MITHNEOS dataset (Binzel et al., 2019), from which the used asteroid reflectances are derived. In this sense the training data has been "contaminated": it includes points possibly quite similar to the test data. In a typical machine learning application, this would indicate a badly designed experiment. However, we would argue that the reflectance of Bennu included in the training data generation is not exactly the same data, the test data being disk-resolved, and the training reflectances disk-integrated. Another argument would be that any asteroid deemed interesting enough for a spacecraft to visit it would likely have been measured by a previous campaign of disk-integrated observations. This is also true for Didymos, the target of the ESA Hera mission: like Bennu, Didymos was included in the MITHNEOS data.

Another reason why results with the OSIRIS-REx OVIRS data were quite good even with lower temperatures may lie in Bennu's low albedo. With low amounts of reflected light, the thermal radiance becomes more prominent and may be easier for the neural network to detect and characterize. Conversely, with lower amounts of reflected light, smaller errors in evaluating the thermal radiance will impair the correction of reflectances. Even if the temperature predictions were without errors, differences in emissivity could skew the predicted spectra to deviate from the ground truth.

Tests with Bennu data were frequently used when evaluating the performance of different network designs. In this sense the network was designed to work with the test data, another common pitfall in developing a machine learning solution. Given the rather fundamental differences between the synthetic training and validation data and the real test data, we saw using the test data this way as necessary. Nevertheless, this makes the neural network suspect of overfitting to the test data.

While the method presented here did work quite well with data from Bennu, several factors call for more testing. Bennu is not representative of all other asteroids, and results from only one asteroid do not provide conclusive evidence. The neural network architecture was also in a sense designed to work with the test data, and it may not perform as well with other data. It is likewise important to consider the accuracy of the OVIRS data used for our tests. While the thermal correction for those measurements is likely more robust than the method presented here, the Bennu data is still corrected with a relatively simple model, and the data considered as ground truth in our tests could contain errors. The tests performed here then do not sufficiently prove the performance and generalizability of the method, and it should be tested with measurements from another asteroid. Unfortunately, to our knowledge data that is suitable for further testing does not yet exist.

ESA's upcoming Hera mission will provide data that could be used to conduct additional tests on the method presented in this study. The ASPECT imaging module on-board Hera's companion CubeSat Milani will record approximately continuous spectra from 0.5 μm to 2.5 μm, near the spectral range of our training data. Hera itself will map the surface temperatures of Didymos and Dimorphos with a thermal infrared imager (TIRI) (Michel et al., 2022). Applying the temperature evaluation method presented in this study to data from ASPECT and comparing the results to temperature maps produced by TIRI would provide more information on how well this method performs with an asteroid very different from Bennu. For additional comparison, the data could also be corrected using the approach taken for OVIRS data of Bennu in Simon et al. (2020).

In its current state, the neural network may not produce correct predictions for the temperatures of shadowed regions, such as those behind larger boulders, or, in the case of twin bodies such as Didymos, the shadow cast by a satellite. Such cases were not intentionally represented in the training data, but some samples with a low albedo, large heliocentric distance, and high temperature may come close. Before applying the neural network to data from Didymos, the neural network has to be retrained using data more representative of the conditions on Didymos, and samples that simulate shadowed regions could also be included. The network could also be familiarized with fresh regolith, as such material was likely uncovered by the DART impact on Dimorphos. Samples analogous to this could possibly be created by simulating reflected radiances using spectral reflectances of meteorites, though changes caused by atmospheric shock and erosion may have rendered meteorite samples unrepresentative of asteroid regolith.

The model used for producing the training data could be described as rather crude and simplistic, in certain aspects even unphysical. As mentioned in Sec. 3.1, the Lommel-Seeliger model of reflection is not suitable for brighter surfaces, or for surfaces that are not flat. Additionally, the model does not consider phase reddening or the opposition surge, other than what may have been present in the used asteroid reflectances. Using a more sophisticated model could improve performance with real data, as it would bring the training data closer to reality. A fairly simple modification would be to exchange the Lommel-Seeliger model for another disk function that is better suited for modeling both dark and bright surfaces. One candidate for this would be a parameterless version of the Akimov disk function (Shkuratov et al., 1999, Eq. 29). Migrating to this model would introduce dependence on the phase angle of a measurement, which could be further accommodated by adding a separate phase function to the pipeline for producing reflected radiances. We suspect the use of the Lommel-Seeliger model was not an issue when testing the network with data from Bennu, an asteroid with a very dark surface. The same model was also utilized for photometric correction of OVIRS measurements in Simon et al. (2020). However, complications could arise when working with lighter asteroids, such as Didymos.

Another simplistic aspect of the data generation is simulating the thermal emission: in our model this has no directional dependence, other than a completely random one from the emissivity. The directional effects of thermal emission are then not tied to the emission angle. The model used for producing thermal radiance spectra also uses an emissivity that is not wavelength dependent, another arguably dubious assumption. While a constant emissivity appears a valid approach for Bennu, it could lead to errors in the case of other asteroids if strong

spectral signatures are expected to be found in the NIR wavelengths. Improving the data generation model while keeping it computationally cheap enough to produce, say, one million data points of a 1000 × 1000 pixel spectral image in a reasonable time would most likely improve the performance of a network trained with this data.

This study aimed to produce a correction method for disk-resolved spectral radiance measurements. However, since the created neural network takes a single spectrum as an input, the same approach could be used to correct disk-integrated observations. This would naturally require the network to be retrained with appropriate data, and such a change to the application and the data would most likely also demand re-optimizing the network architecture. As surveys of disk-integrated asteroid measurements have produced data from a wide variety of asteroids with different orbits and spectral properties, the training data could be gathered from actual measurements instead of simulations. In disk-integrated observations, the thermal emission may also not be sufficiently described by just one temperature value. The temperature is guaranteed to vary across the surface of the observed asteroid, and the observed thermal emission originates from multiple locations with different temperatures. A similar problem could be encountered if this method is applied to data from Milani's ASPECT imaging module, as the longest wavelength channels of this instrument will have a large field-of-view (Michel et al., 2022).

Another expansion for the method could be altering the wavelength range from the current 0.45–2.45 μm, which was chosen largely due to it being the wavelength range of the asteroid reflectance dataset used in generating the training data. Including longer wavelengths would presumably lead to improvements in the performance of the network, especially with lower temperatures. With the current wavelength range, our method is better suited for near-Earth asteroids, which are typically warmer than bodies of the main asteroid belt. If the wavelength range was extended far enough, preferably up to 5 μm, the performance of the network could be tested with data from Dawn and Rosetta. The asteroids targeted by these missions, Ceres, Vesta, Steins, and Lutetia, did not have prominent thermal emission in wavelengths shorter than 3.5 μm (Raponi et al., 2019b, 2019a; Tosi et al., 2014; Leyrat et al., 2011; Keihm et al., 2012). The caveat in moving to other wavelengths is the requirement for approximately continuous spectral reflectances of asteroids in the desired wavelength range, needed to produce suitable training data. These reflectances should also be corrected for thermal excess in the best possible way.

One experiment requiring no new data would be to exclude a number of shorter wavelength channels and attempt to reach similar results. This would lower the requirements for input data, as typically achieving a continuous spectrum from 0.45 μm to 2.45 μm would require fusing together spectral data from multiple sensors. If something goes wrong with this fusion, the resulting spectrum can have extremely sharp drops and rises. Such spectra could confuse a convolution neural network that has only seen smooth features, resulting in an erroneous prediction.

Producing temperature predictions with the neural network was fast, with a 0.5 ms prediction time per sample. For Milani's ASPECT where the NIR instrument is a point spectrometer, this efficiency is not critical, but future missions could employ similar instruments with a frame-based NIR imager. This would greatly increase the number of observations that need to be corrected for thermal emission. If such an instrument were to have the same number of pixels as ASPECT's shorter infrared channels, 640 × 512, the total number of samples to be corrected would be 327 680 for every captured spectral image. Using the temperature prediction method of this study, this would mean a quite manageable computation time of approximately 2.8 min would be needed to produce the temperature predictions.

The speed at which predictions are made could be further increased, possibly quite significantly. The network structure was optimized only for the accuracy of the results, with no thought given to how heavy the computations would be. As a result the network is relatively large, and could likely be streamlined. Further performance improvements could be achieved by implementing the trained network in a lower-level programming language inherently more efficient than Python, such as C. Finally, the predictions were made by running the calculations on a commercial-grade CPU. Using a GPU, which is much better suited for neural network computations, could bring the computation time down substantially. Space-grade GPUs are to our knowledge currently not available, but the popularity of neural networks and other computational methods relying on the parallelization capabilities of GPUs has caused an incentive to bring these components to spacecraft on-board computers (George and Wilson, 2018; Bruhn et al., 2020).

Reducing the computational cost of a correction method is not a priority for missions where the bulk of the computations are carried out on Earth where computational power is not scarce. In the case of CubeSats, the data transmission rate is limited by the low power of the transmission equipment. Missions employing small spacecraft could benefit from processing the data further on the spacecraft's on-board computer and sending only ready data products back to Earth. The on-board computer of a small satellite is naturally quite limited in its computational power, and thus the computations to be run on it should be as efficient as possible.

It is to be noted that processing instrument data on-board a spacecraft also has its dangers. In some cases, this practice can destroy information that could be detected from the raw data with other processing methods. One example of this caveat comes from the analysis of data produced by the Mars Advanced Radar for Subsurface and Ionosphere Sounding (MARSIS) instrument on the Mars Express spacecraft. In this case data processing steps executed on-board the spacecraft before downloading the data to Earth hid evidence of subglacial liquid water deposits under the south pole of Mars (Orosei et al., 2018). Only bypassing the on-board processing and downloading raw data allowed this discovery to be made.

Another concern about the viability of on-board processing is related to the calibration of instruments. While a rigorous calibration procedure is naturally carried out before launch, for some instruments errors in the calibration can become apparent only after months or even years of operation. If this were to happen, and our method of temperature evaluation was to be applied to such data, the produced temperatures could well be erroneous. The error would then propagate to spectral reflectance, which could in turn lead to false results of surface composition. If only the end result of the data processing, the compositional maps, are downloaded to Earth, errors in instrument calibration and their effects will not be found. To alleviate these concerns, we suggest periodically downloading some samples of raw data to be processed under the supervision of a human overseer. These samples could also be processed with methods that are computationally more costly but are known to return accurate results. Comparing results from such methods and from the faster methods employed in computing on an OBC could highlight errors in the on-board processing. Of course, these measures can not be guaranteed to catch all possible errors.

Beyond computational efficiency, the appeal of the method developed in this study lies in the simplicity of its use. One can feed a spectral radiance into the network and receive a prediction for surface temperature, without adjusting any parameters or providing an initial guess for the temperature. The network should be trained again for each target asteroid, but that also requires minimal prior knowledge of the properties of the target: only the perihelion and aphelion distances are needed, and the orbit of an asteroid must at any rate be known well to send a spacecraft to it. A more general solution, a network that works as-is for all asteroid missions without the need to retrain it would be more attractive, but our tests gave worse results for such networks.

Unlike the method used for estimating thermal properties of Vesta in Tosi et al. (2014), our approach does not inherently allow setting constraints on the estimated temperature. Instead, the temperature predictions produced by the network could be clamped to stay within a certain range, with a natural maximum value provided by the blackbody temperature. Information about the target asteroid could also be included before training the network, during the data generation. If the

target is known to have a certain albedo, this value could be used for selecting the minimum and maximum albedos for training and validation data, as well as for maximum temperature evaluation. However, going too far when tuning the data to suit a particular target asteroid may result in more errors if the target happens to not conform to the assumptions made from previous disk-integrated measurements.

5. Conclusions

In this study, a convolution neural network was constructed and trained to predict asteroid surface element temperature from disk-resolved spectral radiance measurements of near-infrared radiation. The temperature predictions were further used to approximate thermally emitted spectral radiances, which were removed from the original spectra to correct them for errors caused by thermal emission. The network was trained and its performance validated during training using synthetic data from a very rudimentary simulator also built during this work. The trained network was tested with real observations of the asteroid Bennu provided by the OVIRS instrument of the OSIRIS-REx mission. To properly characterize the thermal emission, the network would also have to predict a value for emissivity, but attempts at this were unsuccessful.

While the neural network produced promising temperature prediction results from both synthetic data and real measurements of Bennu, we can not declare it ready for deployment in its current state. Testing the network with only Bennu data does not give conclusive evidence for the generalizability of the network performance. Tests with real data from other asteroids would be required, but to our knowledge no real data fitting the specifications for suitable test data exists other than that from Bennu. ESA's upcoming Hera mission is planned to produce such data, but not before 2026. Overall, the method for temperature prediction and thermal correction developed in this study shows promise for missions for which a longer wavelength instrument is not feasible and there is not much prior knowledge of the target body. The method is also computationally efficient, allowing a more careful implementation of it to possibly be run on the on-board computers of future nanosatellite missions.

Author statement

Leevi Lind: Conceptualization, Methodology, Software, Formal analysis, Investigation, Writing - Original Draft, Writing - Review & Editing.

Antti Penttilä: Methodology, Formal analysis, Writing - Review & Editing.

Kimmo A. Riihiaho: Methodology, Software, Formal analysis, Writing - Review & Editing.

Eric MacLennan: Methodology, Formal analysis, Writing - Review & Editing.

Ilkka Pölönen: Conceptualization, Methodology, Software, Formal analysis, Writing - Review & Editing, Supervision, Project administration, Funding acquisition.

Funding

This work was funded by the Smart–HSI project of the Academy of Finland (grant number 335615).

Code and data availability

All program code and the weights for the final trained neural network are available on GitHub at https://github.com/silmae/AsTherCorNN under the MIT license.

The training and validation data produced and used in this research is available upon request. As a derivative of an unlicensed dataset, it can not be made public.

The test data consisting of OVIRS observations of Bennu is to our knowledge currently not publicly available in the form it was used for this study.

Declaration of competing interest

The authors declare that they have no known competing financial interests or personal relationships that could have appeared to influence the work reported in this paper.

Acknowledgments

We would like to thank Dr. Amy A. Simon of the NASA Goddard Space Flight Center for providing us with OVIRS data of Bennu.

We also thank Fabi Prezja for numerous helpful discussions regarding neural networks.

Additionally, we thank the two anonymous reviewers whose comments greatly improved this paper.

References

2000 ASTM standard extraterrestrial spectrum reference e-490-00. URL https://www.nrel.gov/grid/solar-resource/spectra-astm-e490.html. (Accessed 1 November 2022).

Abadi, M., Agarwal, A., Barham, P., Brevdo, E., Chen, Z., Citro, C., Corrado, G.S., Davis, A., Dean, J., Devin, M., Ghemawat, S., Goodfellow, I., Harp, A., Irving, G., Isard, M., Jia, Y., Jozefowicz, R., Kaiser, L., Kudlur, M., Levenberg, J., Mané, D., Monga, R., Moore, S., Murray, D., Olah, C., Schuster, M., Shlens, J., Steiner, B., Sutskever, I., Talwar, K., Tucker, P., Vanhoucke, V., Vasudevan, V., Viégas, F., Vinyals, O., Warden, P., Wattenberg, M., Wicke, M., Yu, Y., Zheng, X., 2015. TensorFlow: large-scale machine learning on heterogeneous systems. https://www.tensorflow.org/.softwareavailablefromtensorflow.org. URL.

Annala, L., Honkavaara, E., Tuominen, S., Pölönen, I., 2020. Chlorophyll concentration retrieval by training convolutional neural network for stochastic model of leaf optical properties (SLOP) inversion. In: Remote Sensing, vol. 12. Multidisciplinary Digital Publishing Institute, p. 283. URL: https://www.mdpi.com/2072-4292/12/2/283, 10.3390/rs12020283.

Ball, N.M., Brunner, R.J., 2010. Data mining and machine learning in astronomy. In: International Journal of Modern Physics D, vol. 19. World Scientific Publishing Co, pp. 1049–1106. URL: https://www.worldscientific.com/doi/abs/10.1142/S0218271810017160, 10.1142/S0218271810017160.

Bennu on Small-Body Database. URL https://ssd.jpl.nasa.gov/tools/sbdb_lookup.html#/?sstr=bennu. (Accessed 6 April 2022).

Binzel, R., DeMeo, F., Turtelboom, E., Bus, S., Tokunaga, A., Burbine, T., Lantz, C., Polishook, D., Carry, B., Morbidelli, A., Birlan, M., Vernazza, P., Burt, B., Moskovitz, N., Slivan, S., Thomas, C., Rivkin, A., Hicks, M., Dunn, T., Reddy, V., Sanchez, J., Granvik, M., Kohout, T., 2019. Compositional distributions and evolutionary processes for the near-Earth object population: results from the MIT-Hawaii Near-Earth Object Spectroscopic Survey (MITHNEOS). Icarus 324, 41–76. URL: https://linkinghub.elsevier.com/retrieve/pii/S0019103518302124, 10.1016/j.icarus.2018.12.035.

Bruhn, F.C., Tsog, N., Kunkel, F., Flordal, O., Troxel, I., 2020. Enabling radiation tolerant heterogeneous GPU-based onboard data processing in space. CEAS Space Journal 12, 551–564. https://doi.org/10.1007/s12567-020-00321-9, 10.1007/s12567-020-00321-9.

Chollet, F., et al., 2015. Keras. https://keras.io.

Christensen, P.R., Hamilton, V.E., Mehall, G.L., Pelham, D., O'Donnell, W., Anwar, S., Bowles, H., Chase, S., Fahlgren, J., Farkas, Z., Fisher, T., James, O., Kubik, I., Lazbin, I., Miner, M., Rassas, M., Schulze, L., Shamordola, K., Tourville, T., West, G., Woodward, R., Lauretta, D., 2018. The OSIRIS-REx thermal emission spectrometer (OTES) instrument. Space Sci. Rev. 214, 87. https://doi.org/10.1007/s11214-018-0513-6, 10.1007/s11214-018-0513-6.

Coradini, A., Capaccioni, F., Erard, S., Arnold, G., De Sanctis, M.C., Filacchione, G., Tosi, F., Barucci, M.A., Capria, M.T., Ammannito, E., Grassi, D., Piccioni, G., Giuppi, S., Bellucci, G., Benkhoff, J., Bibring, J.P., Blanco, A., Blecka, M., Bockelee-Morvan, D., Carraro, F., Carlson, R., Carsenty, U., Cerroni, P., Colangeli, L., Combes, M., Combi, M., Crovisier, J., Drossart, P., Encrenaz, E.T., Federico, C., Fink, U., Fonti, S., Giacomini, L., Ip, W.H., Jaumann, R., Kuehrt, E., Langevin, Y., Magni, G., McCord, T., Mennella, V., Mottola, S., Neukum, G., Orofino, V., Palumbo, P., Schade, U., Schmitt, B., Taylor, F., Tiphene, D., Tozzi, G., 2011. The surface composition and temperature of asteroid 21 Lutetia as observed by Rosetta/VIRTIS. In: Science, vol. 334. American Association for the Advancement of Science, pp. 492–494. URL: https://www.science.org/doi/10.1126/science.1204062, 10.1126/science.1204062.

De Sanctis, M.C., Coradini, A., Ammannito, E., Filacchione, G., Capria, M.T., Fonte, S., Magni, G., Barbis, A., Bini, A., Dami, M., Ficai-Veltroni, I., Preti, G., VIR Team, 2011. The VIR spectrometer. Space Sci. Rev. 163, 329–369. https://doi.org/10.1007/s11214-010-9668-5, 10.1007/s11214-010-9668-5.

Delbo, M., Mueller, M., Emery, J.P., Rozitis, B., Capria, M.T., 2015. Asteroid Thermophysical Modeling. University of Arizona Press, pp. 107–128. URL: http://www.jstor.org/stable/j.ctt18gzdvc.12.

DeMeo, F.E., Carry, B., 2013. The taxonomic distribution of asteroids from multi-filter all-sky photometric surveys. Icarus 226, 723–741. URL: https://www.sciencedirect.com/science/article/pii/S0019103513002923, 10. 1016/j.icarus.2013.06.027.

DeMeo, F.E., Binzel, R.P., Slivan, S.M., Bus, S.J., 2009. An extension of the Bus asteroid taxonomy into the near-infrared. Icarus 202, 160–180. URL: https://www.sciencedirect.com/science/article/pii/S0019103509000554, 10. 1016/j.icarus.2009.02.005.

Ferrari, F., Franzese, V., Pugliatti, M., Giordano, C., Topputo, F., 2021. Preliminary mission profile of Hera's Milani CubeSat. Adv. Space Res. 67, 2010–2029. URL: https://www.sciencedirect.com/science/article/pii/S0273117720309078. URL: 10.1016/j.asr.2020.12.034.

Gaffey, M.J., 1993. Asteroid spectroscopy: progress and perspectives. Meteoritics 28, 161–187. https://doi.org/10.1111/j.1945-5100.1993.tb00755.x.

George, A.D., Wilson, C.M., 2018. Onboard processing with hybrid and reconfigurable computing on small satellites. In: Proceedings of the IEEE, vol. 106, pp. 458–470. https://doi.org/10.1109/JPROC.2018.2802438.

Goldberg, H., Karatekin, Ö., Ritter, B., Herique, A., Tortora, P., Prioroc, C., Gutierrez, B., Martino, P., Carnelli, I., 2019. The juventas CubeSat in support of ESA's hera mission to the asteroid didymos. In: Small Satellite Conference. URL: https://digitalcommons.usu.edu/smallsat/2019/all2019/73.

Goodfellow, I., Bengio, Y., Courville, A., 2016. Deep Learning. Adaptive Computation and Machine Learning Series. MIT Press, Cambridge, MA, USA.

Hakala, T., Pölönen, I., Honkavaara, E., Näsi, R., Hakala, T., Lindfors, A., 2020. Using aerial platforms in predicting water quality parameters from hyperspectral imaging data with deep neural networks. Cham. Computational Methods in Applied Sciences. In: Diez, P., Neittaanmäki, P., Periaux, J., Tuovinen, T., Pons-Prats, J. (Eds.), Computation and Big Data for Transport: Digital Innovations in Surface and Air Transport Systems. Springer International Publishing, pp. 213–238. https://doi.org/10.1007/978-3-030-37752-6_13, 10.1007/978-3-030-37752-6_13.

Hapke, B., 2012. Theory of Reflectance and Emittance Spectroscopy, second ed. Cambridge University Press, Cambridge https://www.cambridge.org/core/books/theory-of-reflectance-and-emittance-spectroscopy/C266E1164D5E14DA18141F03D0E0EAB0. 10.1017/CBO9781139025683.

Iwata, T., Kitazato, K., Abe, M., Ohtake, M., Arai, T., Arai, T., Hirata, N., Hiroi, T., Honda, C., Imae, N., Komatsu, M., Matsunaga, T., Matsuoka, M., Matsuura, S., Nakamura, T., Nakato, A., Nakauchi, Y., Osawa, T., Senshu, H., Takagi, Y., Tsumura, K., Takato, N., Watanabe, S.i., Barucci, M.A., Palomba, E., Ozaki, M., 2017. NIRS3: the near infrared spectrometer on Hayabusa2. Space Sci. Rev. 208, 317–337. https://doi.org/10.1007/s11214-017-0341-0, 10.1007/s11214-017-0341-0.

Keihm, S., Tosi, F., Kamp, L., Capaccioni, F., Gulkis, S., Grassi, D., Hofstadter, M., Filacchione, G., Lee, S., Giuppi, S., Janssen, M., Capria, M., 2012. Interpretation of combined infrared, submillimeter, and millimeter thermal flux data obtained during the Rosetta fly-by of Asteroid (21) Lutetia. Icarus 221, 395–404. URL: https://www.sciencedirect.com/science/article/pii/S001910351200320X, 10. 1016/j.icarus.2012.08.002.

Kingma, D.P., Ba, J., 2017. Adam: a method for stochastic optimization. URL: http://arxiv.org/abs/1412.6980. arXiv:1412.6980 [cs].

Kitazato, K., Clark, B.E., Abe, M., Abe, S., Takagi, Y., Hiroi, T., Barnouin-Jha, O.S., Abell, P.A., Lederer, S.M., Vilas, F., 2008. Near-infrared spectrophotometry of asteroid 25143 itokawa from NIRS on the Hayabusa spacecraft. Icarus 194, 137–145. URL: https://www.sciencedirect.com/science/article/pii/S0019103507003764, 10. 1016/j.icarus.2007.08.029.

Kitazato, K., Milliken, R.E., Iwata, T., Abe, M., Ohtake, M., Matsuura, S., Arai, T., Nakauchi, Y., Nakamura, T., Matsuoka, M., Senshu, H., Hirata, N., Hiroi, T., Pilorget, C., Brunetto, R., Poulet, F., Riu, L., Bibring, J.P., Takir, D., Domingue, D.L., Vilas, F., Barucci, M.A., Perna, D., Palomba, E., Galiano, A., Tsumura, K., Osawa, T., Komatsu, M., Nakato, A., Arai, T., Takato, N., Matsunaga, T., Takagi, Y., Matsumoto, K., Kouyama, T., Yokota, Y., Tatsumi, E., Sakatani, N., Yamamoto, Y., Okada, T., Sugita, S., Honda, R., Morota, T., Kameda, S., Sawada, H., Honda, C., Yamada, M., Suzuki, H., Yoshioka, K., Hayakawa, M., Ogawa, K., Cho, Y., Shirai, K., Shimaki, Y., Hirata, N., Yamaguchi, A., Ogawa, N., Terui, F., Yamaguchi, T., Takei, Y., Saiki, T., Nakazawa, S., Tanaka, S., Yoshikawa, M., Watanabe, S., Tsuda, Y., 2019. The surface composition of asteroid 162173 Ryugu from Hayabusa2 near-infrared spectroscopy. In: Science, vol. 364. American Association for the Advancement of Science, pp. 272–275. URL: https://www.science.org/lookup/doi/10.1126/science.aav7432, 10.1126/science.aav7432.

Kopp, G., Lean, J.L., 2011. A new, lower value of total solar irradiance: evidence and climate significance. Geophys. Res. Lett. 38. URL: https://onlinelibrary.wiley.com/doi/abs/10.1029/2010GL045777 https://onlinelibrary.wiley.com/doi/pdf/10.1029/2010GL045777, 10. 1029/2010GL045777.

Korda, D., Penttilä, A., Klami, A., Kohout, T., 2023. Neural network for determining an asteroid mineral composition from reflectance spectra. In: Astronomy & Astrophysics, vol. 669. EDP Sciences, p. A101. URL: https://www.aanda.org/articles/aa/abs/2023/01/aa43886-22/aa43886-22.html, 10.1051/0004-6361/202243886.

Kruse, F.A., Lefkoff, A.B., Boardman, J.W., Heidebrecht, K.B., Shapiro, A.T., Barloon, P.J., Goetz, A.F.H., 1993. The spectral image processing system (SIPS)—interactive visualization and analysis of imaging spectrometer data. Remote Sens. Environ. 44, 145–163. URL: https://www.sciencedirect.com/science/article/pii/003442579390013N, 10.1016/0034-4257(93)90013-N.

Leyrat, C., Coradini, A., Erard, S., Capaccioni, F., Capria, M.T., Drossart, P., Sanctis, M.C.D., Tosi, F., Team, V., 2011. Thermal properties of the asteroid (2867) Steins as observed by VIRTIS/Rosetta. In: Astronomy & Astrophysics, vol. 531. EDP Sciences, p. A168. URL: https://www.aanda.org/articles/aa/abs/2011/07/aa16529-11/aa16529-11.html, 10.1051/0004-6361/201116529.

Michel, P., Küppers, M., Bagatin, A.C., Carry, B., Charnoz, S., Leon, J.d., Fitzsimmons, A., Gordo, P., Green, S.F., Hérique, A., Juzi, M., Karatekin, Ö., Kohout, T., Lazzarin, M., Murdoch, N., Okada, T., Palomba, E., Pravec, P., Snodgrass, C., Tortora, P., Tsiganis, K., Ulamec, S., Vincent, J.B., Wünnemann, K., Zhang, Y., Raducan, S.D., Dotto, E., Chabot, N., Cheng, A.F., Rivkin, A., Barnouin, O., Ernst, C., Stickle, A., Richardson, D.C., Thomas, C., Arakawa, M., Miyamoto, H., Nakamura, A., Sugita, S., Yoshikawa, M., Abell, P., Asphaug, E., Ballouz, R.L., Bottke, W.F., Lauretta, D.S., Walsh, K.J., Martino, P., Carnelli, I., 2022. The ESA hera mission: detailed characterization of the DART impact outcome and of the binary asteroid (65803) didymos. In: The Planetary Science Journal, vol. 3. IOP Publishing, p. 160. URL: https://iopscience.iop.org/article/10.3847/PSJ/ac6f52/meta, 10.3847/PSJ/ac6f52.

Modest, M.F., 2013. Radiative Heat Transfer, third ed. Academic Press, New York. OCLC: ocn813855549.

Myhrvold, N., 2018. Asteroid thermal modeling in the presence of reflected sunlight. Icarus 303, 91–113. URL: https://linkinghub.elsevier.com/retrieve/pii/S0019103516307631, 10.1016/j.icarus.2017.12.024.

Nair, V., Hinton, G.E., 2010. Rectified linear units improve restricted Boltzmann machines. In: Proceedings of the 27th International Conference on International Conference on Machine Learning. Omnipress, Madison, WI, USA, pp. 807–814.

Orosei, R., Lauro, S.E., Pettinelli, E., Cicchetti, A., Coradini, M., Cosciotti, B., Di Paolo, F., Flamini, E., Mattei, E., Pajola, M., Soldovieri, F., Cartacci, M., Cassenti, F., Frigeri, A., Giuppi, S., Martufi, R., Masdea, A., Mitri, G., Nenna, C., Noschese, R., Restano, M., Seu, R., 2018. Radar evidence of subglacial liquid water on Mars. In: Science, vol. 361. American Association for the Advancement of Science, pp. 490–493. URL: https://www.science.org/doi/10.1126/science.aar7268, 10. 1126/science.aar7268.

O'Malley, T., Bursztein, E., Long, J., Chollet, F., Jin, H., Invernizzi, L., et al., 2019. Kerastuner. https://github.com/keras-team/keras-tuner.

Pelivan, I., Drube, L., Kührt, E., Helbert, J., Biele, J., Maibaum, M., Cozzoni, B., Lommatsch, V., 2017. Thermophysical modeling of didymos' moon for the asteroid impact mission. Adv. Space Res. 59, 1936–1949. URL: https://www.sciencedirect.com/science/article/pii/S0273117717300224, 10. 1016/j.asr.2016.12.041.

Penttilä, A., Hietala, H., Muinonen, K., 2021. Asteroid spectral taxonomy using neural networks. In: Astronomy & Astrophysics, vol. 649. EDP Sciences, p. A46. URL: https://www.aanda.org/articles/aa/abs/2021/05/aa38545-20/aa38545-20.html, 10.1051/0004-6361/202038545.

Prockter, L., Murchie, S., Cheng, A., Krimigis, S., Farquhar, R., Santo, A., Trombka, J., 2002. The NEAR shoemaker mission to asteroid 433 eros. Acta Astronaut. 51, 491–500. URL: https://www.sciencedirect.com/science/article/pii/S009457650200098X, 10. 1016/S0094-5765(02)00098-X.

Python 3.9.7 documentation. URL: https://docs.python.org/release/3.9.7. (Accessed 5 January 2023).

Raponi, A., Carrozzo, F.G., Zambon, F., De Sanctis, M.C., Ciarniello, M., Frigeri, A., Ammannito, E., Tosi, F., Combe, J.P., Longobardo, A., Palomba, E., Pieters, C.M., Raymond, C.A., Russell, C.T., 2019a. Mineralogical mapping of Coniraya quadrangle of the dwarf planet Ceres. Icarus 318, 99–110. URL: https://www.sciencedirect.com/science/article/pii/S0019103517303317, 10. 1016/j.icarus.2017.10.023.

Raponi, A., De Sanctis, M.C., Carrozzo, F.G., Ciarniello, M., Castillo-Rogez, J.C., Ammannito, E., Frigeri, A., Longobardo, A., Palomba, E., Tosi, F., Zambon, F., Raymond, C.A., Russell, C.T., 2019b. Mineralogy of Occator crater on Ceres and insight into its evolution from the properties of carbonates, phyllosilicates, and chlorides. Icarus 320, 83–96. URL: https://www.sciencedirect.com/science/article/pii/S0019103517305535, 10. 1016/j.icarus.2018.02.001.

Reddy, V., Gaffey, M.J., Abell, P.A., Hardersen, P.S., 2012. Constraining albedo, diameter and composition of near-Earth asteroids via near-infrared spectroscopy. Icarus 219, 382–392. URL: https://www.sciencedirect.com/science/article/pii/S0019103512000905, 10. 1016/j.icarus.2012.03.005.

Reuter, D.C., Simon, A.A., Hair, J., Lunsford, A., Manthripragada, S., Bly, V., Bos, B., Brambora, C., Caldwell, E., Casto, G., Dolch, Z., Finneran, P., Jennings, D., Jhabvala, M., Matson, E., McLelland, M., Roher, W., Sullivan, T., Weigle, E., Wen, Y., Wilson, D., Lauretta, D.S., 2018. The OSIRIS-REx visible and InfraRed spectrometer (OVIRS): spectral maps of the asteroid Bennu. Space Sci. Rev. 214, 54. URL: http://link.springer.com/10.1007/s11214-018-0482-9, 10.1007/s11214-018-0482-9.

Rivkin, A., Binzel, R., Bus, S., 2005. Constraining near-Earth object albedos using near-infrared spectroscopy. Icarus 175, 175–180. URL: https://linkinghub.elsevier.com/retrieve/pii/S0019103504003951, 10.1016/j.icarus.2004.11.005.

Rivkin, A.S., Chabot, N.L., Stickle, A.M., Thomas, C.A., Richardson, D.C., Barnouin, O., Fahnestock, E.G., Ernst, C.M., Cheng, A.F., Chesley, S., Naidu, S., Statler, T.S., Barbee, B., Agrusa, H., Moskovitz, N., Daly, R.T., Pravec, P., Scheirich, P., Dotto, E., Corte, V.D., Michel, P., Küppers, M., Atchison, J., Hirabayashi, M., 2021. The double asteroid redirection test (DART): planetary defense investigations and requirements. In: The Planetary Science Journal, vol. 2. IOP Publishing, p. 173. URL: https://iopscience.iop.org/article/10.3847/PSJ/ac063e/meta, 10.3847/PSJ/ac063e.

Rognini, E., Capria, M.T., Tosi, F., De Sanctis, M.C., Ciarniello, M., Longobardo, A., Carrozzo, F.G., Raponi, A., Frigeri, A., Palomba, E., Fonte, S., Giardino, M., Ammannito, E., Raymond, C.A., Russell, C.T., 2020. High thermal inertia zones on Ceres from Dawn data. J. Geophys. Res.: Planets 125, e2018JE005733. URL: https://onlinelibrary.wiley.com/doi/abs/10.1029/2018JE005733 https://onlinelibrary.wiley.com/doi/pdf/10.1029/2018JE005733, 10. 1029/2018JE005733.

Ryan, E.L., Woodward, C.E., 2010. Rectified asteroid albedos and diameters from *IRAS* and *MSX* photometry catalogs. In: The Astronomical Journal, vol. 140. American Astronomical Society, pp. 933–943. https://doi.org/10.1088/0004-6256/140/4/933, 10. 1088/0004-6256/140/4/933.

Shepard, M.K., 2017. Introduction to Planetary Photometry. Cambridge University Press, Cambridge. URL: https://www.cambridge.org/core/books/introduction-to-planetary-photometry/EB8DD2E334CA395105856AF704E11117, 10.1017/9781316443545.

Shkuratov, Y.G., Kreslavsky, M.A., Ovcharenko, A.A., Stankevich, D.G., Zubko, E.S., Pieters, C., Arnold, G., 1999. Opposition effect from clementine data and mechanisms

of backscatter. Icarus 141, 132–155. URL: https://www.sciencedirect.com/science/article/pii/S0019103599961547, 10. 1006/icar.1999.6154.

Simon, A.A., Kaplan, H.H., Hamilton, V.E., Lauretta, D.S., Campins, H., Emery, J.P., Barucci, M.A., DellaGiustina, D.N., Reuter, D.C., Sandford, S.A., Golish, D.R., Lim, L.F., Ryan, A., Rozitis, B., Bennett, C.A., 2020. Widespread carbon-bearing materials on near-Earth asteroid (101955) Bennu. In: Science, vol. 370. American Association for the Advancement of Science, eabc3522. URL: https://www.science.org/doi/10.1126/science.abc3522, 10. 1126/science.abc3522.

Topputo, F., Wang, Y., Giordano, C., Franzese, V., Goldberg, H., Perez-Lissi, F., Walker, R., 2021. Envelop of reachable asteroids by M-ARGO CubeSat. Adv. Space Res. 67, 4193–4221. URL: https://www.sciencedirect.com/science/article/pii/S0273117721001782, 10. 1016/j.asr.2021.02.031.

Tosi, F., Capria, M.T., De Sanctis, M.C., Combe, J.P., Zambon, F., Nathues, A., Schröder, S.E., Li, J.Y., Palomba, E., Longobardo, A., Blewett, D.T., Denevi, B.W., Palmer, E., Capaccioni, F., Ammannito, E., Titus, T.M., Mittlefehldt, D.W., Sunshine, J.M., Russell, C.T., Raymond, C.A., 2014. Thermal measurements of dark and bright surface features on Vesta as derived from Dawn/VIR. Icarus 240, 36–57. URL: https://www.sciencedirect.com/science/article/pii/S0019103514001432, 10. 1016/j.icarus.2014.03.017.

Walker, R., Binns, D., Bramanti, C., Casasco, M., Concari, P., Izzo, D., Feili, D., Fernandez, P., Fernandez, J.G., Hager, P., Koschny, D., Pesquita, V., Wallace, N., Carnelli, I., Khan, M., Scoubeau, M., Taubert, D., 2018. Deep-space CubeSats: thinking inside the box. Astron. Geophys. 59. https://doi.org/10.1093/astrogeo/aty232, 5.24–5.30 10.1093/astrogeo/aty232.